Available online at www.sciencedirect.com
ScienceDirect
Journal of the European Ceramic Society 31 (2011) 1339–1344
www.elsevier.com/locate/jeurceramsoc

Processing and mechanical behavior at elevated temperatures of directionally solidified proton conducting perovskites

M.J. López-Robledo [a,1], C. Vaquero-Aguilar [a], J. Martínez-Fernández [a], J.I. Peña [b], A. Sayir [c], M. Jiménez-Melendo [a,*]

[a] *Departamento de Física de la Materia Condensada, Universidad de Sevilla, Aptdo. 1065, 41080 Sevilla, Spain*
[b] *Instituto de Ciencia de Materiales de Aragón (ICMA), Universidad de Zaragoza-CSIC, 50009 Zaragoza, Spain*
[c] *NASA-Glenn Research Center, Lewis Field, 21000 Brookpark Road, Mail Stop 106-1, Cleveland, OH 44135-3191, USA*

Available online 26 June 2010

Abstract

High-temperature proton conducting perovskite oxides have been fabricated by directional solidification using a laser-heated floating zone (LHFZ) method. Several families of compositions were selected: $SrCe_{1-x}Y_xO_{3-\delta}$ (with $x = 0.1$, 0.2), $BaCe_{1-x}M_xO_{3-\delta}$ (with M = Y, Yb and Ca; $x = 0.05$, 0.2), $Sr_3Ca_{1.18}Nb_{1.82}O_{9-\delta}$, $SrZr_{0.8}Y_{0.2}O_{3-\delta}$ and $SrTi_{0.95}Sc_{0.05}O_{3-\delta}$. The resulting microstructures were characterized by electron microscopy and X-ray diffraction. The compounds exhibit a singular microstructure consisting of strongly textured crystalline cells surrounded by an intercellular amorphous phase. Compressive mechanical tests were performed at elevated temperatures in air at constant strain rate to evaluate the creep resistance. The results are discussed in terms of ionic radius, degree of aliovalence and content of dopant cations.

Keywords: Perovskites; Plasticity; Microstructure-final; Fuel cells; Directional solidification

1. Introduction

Solid oxide fuel cells (SOFCs) are attracting considerable interest as alternative energy conversion devices due to their high efficiencies and low emissions. They are currently based on anionic solid conductors, mostly yttria-stabilized zirconia. In the last years, however, high-temperature protonic conductors (HTPC) are being considered for use as electrolyte materials in SOFCs.[1–5] Perovskite-structured oxides of generic formula ABO_3, where A^{2+} and B^{4+} denote site cations (such as $BaCeO_3$ or $SrCeO_3$), seem to be particularly suitable for this purpose because of its high proton conducting performance, in addition to a good oxygen-ion conductivity.[6–13] The partial substitution of the B-site cations by an aliovalent cation (such as Y^{3+} or Ca^{2+}) creates oxygen vacancies in the oxygen sublattice due to charge compensation. In Y-doped $BaCeO_3$, for instance, the defect reaction in Kröger–Vink notation is:

$$Y_2O_3 \rightarrow 2Y'_{Ce} + 3O_O^x + V_O^{\bullet\bullet} \quad (1)$$

By treatment in water vapour at high temperatures, protons replace oxygen vacancies as charge-compensators for the acceptor dopants:

$$H_2O(g) + V_O^{\bullet\bullet} + O_O^x \rightarrow 2OH^{\bullet} \quad (2)$$

The defect is described as a hydroxyl group because the interstitial proton is closely associated with the neighbouring oxygen ion. Mixed perovskites of formula $A_3B'B''_2O_{9-\delta}$, where A and B′ are divalent and B″ pentavalent cations, have also become of interest because oxygen vacancies can be created by varying the B′/B″ ratio.

Doped perovskite oxides have therefore been extensively studied in order to improve oxygen-ion and proton conductivity and chemical stability.[1–14] Most of the studies have been performed on sintered or hot-pressed compounds. However, directionally solidified materials grown from the melt through a controlled system have been shown to exhibit properties superior to their polycrystalline counterparts,[15–17] due to the unique microstructures that can be created during directional solidification. Among the various directional solidification techniques, the laser-heated floating zone (LHFZ) has been proved to be a fast and effective technique that produces materials in a variety of processing conditions and shapes.[18–21] This processing method generates very high thermal gradients within the mate-

* Corresponding author. Tel.: +34 954550938; fax: +34 954552870.
E-mail address: melendo@us.es (M. Jiménez-Melendo).
[1] Permanent address: Departamento de Sistemas Físicos, Químicos y Naturales, Universidad Pablo de Olavide, Ctra. Utrera, km 1, 41013 Sevilla, Spain.

0955-2219/$ – see front matter © 2010 Elsevier Ltd. All rights reserved.
doi:10.1016/j.jeurceramsoc.2010.05.022

rial, which are responsible for some of the novel microstructural features attainable.[22]

In this paper, the LHFZ method has been used to produce a variety of families and compositions of directionally solidified high-temperature proton conducting perovskites: $SrCe_{1-x}Y_xO_{3-\delta}$ (with $x = 0.1$, 0.2), $BaCe_{1-x}M_xO_{3-\delta}$ (with M = Y, Yb and Ca; $x = 0.05$, 0.2), $SrZr_{0.8}Y_{0.2}O_{3-\delta}$, $SrTi_{0.95}Sc_{0.05}O_{3-\delta}$ and $Sr_3Ca_{1.18}Nb_{1.82}O_{9-\delta}$. The structural and microstructural characteristics have been investigated by X-ray diffraction and electron microscopy. Preliminary deformation tests were performed at elevated temperatures in air at constant strain rate in order to assess the relative strengths of the various materials. The mechanical data have been correlated with ionic radius and concentration of the aliovalent dopant cations.

2. Experimental details

Crystals have been directionally solidified using the LHFZ method described elsewhere.[16,22] The polycrystalline precursors were prepared by solid state reaction of CeO_2 (99.0% pure), BaO (99.9%), Y_2O_3 (99.9%), Yb_2O_3 (99.9%) and CaO (99.9%) powders, supplied by Sigma–Aldrich, and $SrCO_3$ (99.999%) and Nb_2O_5 (99.9%) supplied by CERAC. Firstly, the raw powders were mixed in the required stoichiometric ratio and grounded in WC media for 1 h at 400 rpm using a centrifugal ball mill. The resulting powders were calcined for 10 h at 1200 °C in air, and then carefully regrounded. Finally, the powders were uniaxially pressed at 150 MPa and then isostatically cold pressed at 210 MPa to produce polycrystalline rods that were sintered in alumina crucibles for 10 h at 1500 °C in air. These rods, with a diameter of 4–5 mm, were used as precursors for the laser-heated floating zone apparatus.

The LHFZ system used a CO_2 laser split in two beams 180° apart from each other. Each beam was focused using ZnSe lenses into the topmost end of the polycrystalline precursor until a molten drop was formed. Then, an almost fully dense (99.9% of theoretical density) and large-grained (100 μm) polycrystalline Al_2O_3 seed was slowly brought near the precursor until it was wetted by the molten drop previously formed. The molten zone was thus maintained by surface tension between both solids (floating zone). The precursor was moved vertically through the beam incidence area, being continuously melted and solidified. Only a small fraction of the laser maximum power (2200 W) was used due to the high absorption of the oxides to 10.6 μm radiation. Although the exact temperature of the molten zone could not be determined because of the lack of melt emissivity data, it was estimated to oscillate between 1900 and 2000 °C in the hottest zone (centre of the melt). The doped barium cerates were grown in the ICMA (Instituto de Ciencia de Materiales de Aragón, Zaragoza, Spain) at 300 mm/h and a rotation rate of 50 revolutions per minute. The other compositions were grown in the NASA-Glenn Research Center (Cleveland, OH, USA) using a travel rate of 500 mm/h without rotation. After the LHFZ process, cylinders with a typical length of 50–100 mm and a diameter of 3–4 mm were obtained. Several crystals were grown directly from the precursor rods without the use of alumina seeds.

The microstructural characterization of the as-fabricated and deformed compounds was carried out using scanning (SEM) and transmission (TEM) electron microscopy (Microscopy Service, University of Sevilla, Spain). For SEM observations, transverse and longitudinal cross-sections were cut from the samples using a low-speed diamond saw and mechanically polished using up to 0.25 μm grade diamond paste. Energy-dispersive X-ray (EDX) microanalysis was also performed on the specimens during SEM observation. TEM foils were prepared by conventional techniques of grinding, dimpling and ion-milling. No conductive coating was required for microscopy observations due to the good electronic conductivity of the materials. The crystalline structure of the as-fabricated perovskites was investigated by powder X-ray diffraction (XRD).

After the LHFZ process, cylindrical samples of 4–5 mm in length parallel to the growth axis were cut from the as-fabricated compounds with a low-speed diamond saw and used for mechanical testing. This relatively low height to width ratio was chosen to avoid the bending of the specimens during testing due to irregularities in the sample diameter. Compression tests were carried out at a temperature T of 1300 °C in air at a constant crosshead speed of 1 μm/min (corresponding to an initial strain rate of about 4×10^{-6} s^{-1}). Lower temperatures and/or higher strain rates led to catastrophic failure of the samples without any plastic deformation. The recorded data, load versus time, were plotted as σ–ε curves, where σ is the true stress and ε the true strain.

3. Results and discussion

3.1. Microstructural characterization

XRD studies showed that all the directionally solidified crystals produced by the LHFZ method have an orthorhombic structure with Pnma space group, as found in most distorted perovskite oxides.[16,23] XRD analyses also showed that the average volume of the unit cells decreases with increasing dopant content in $SrCe_{1-x}Y_xO_{3-\delta}$ and $BaCe_{1-x}Y_xO_{3-\delta}$. The same variation of unit cell volume with doping has been previously reported on sintered polycrystals of similar compositions produced by solid state reaction.[24,25] This result suggests that the volume expansion caused by the substitution of Y^{3+} in the Ce^{4+} sites due to differences in ionic radii is overcome by the volume contraction caused by the formation of oxygen vacancies that accompanies yttrium doping (Eq. (1)). However, other effects such as cooperative BO_6 octahedral rotation and distortion, A-sites antiparallel shift, dopant partitioning over both A and B sites and formation of complex defects are concurrent with doping,[25,26] thus precluding a simple linkage between Y content and unit cell volume.

The directionally solidified materials exhibit a singular microstructure, with characteristics in between those of single and polycrystals. Fig. 1 shows typical SEM micrographs of transverse cross-sections of calcium-doped $BaCeO_3$ with two different compositions. The microstructure consists of strongly textured cells (grains) surrounded by a secondary intergranular phase. TEM selected area diffraction revealed that the cells were crystalline, in agreement with XRD studies, and that

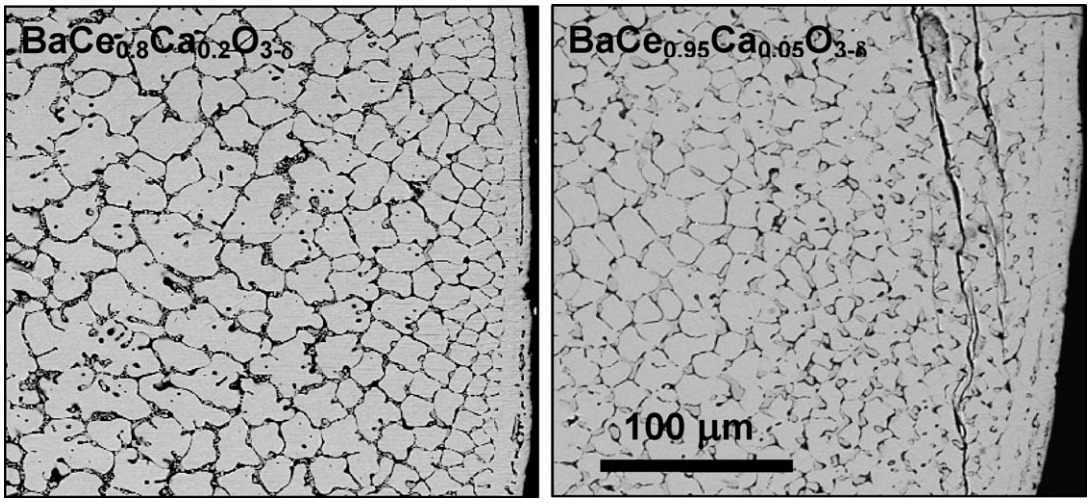

Fig. 1. SEM micrographs of transversal sections of as-fabricated $BaCeO_3$ doped with two different calcium contents. Cell size decreases with increasing radial distance from the growth axis.

the intergranular phase was amorphous. An extensive study of the internal microstructure of the cells in $SrCe_{1-x}Y_xO_{3-\delta}$ has been presented elsewhere.[16,27] Fig. 1 also shows that the cells decrease continuously in size with increasing the radial distance from the centre of the sample (growth axis) towards the external surface. This feature is common to materials produced by the LHFZ method, and is caused by the large radial temperature gradients established at the solid/liquid interface, which lead to growth fronts that are not completely flat. The same trend was found for the amorphous phase, as shown in Fig. 2 for Ca- and Y-doped $BaCeO_3$ and Y-doped $SrCeO_3$; the surface fraction occupied by the secondary phase decreases when moving from the axis growth to the external surface. Moreover, both the cells and the amorphous phase increase in size with increasing dopant concentration in the same compound (Figs. 1 and 2).

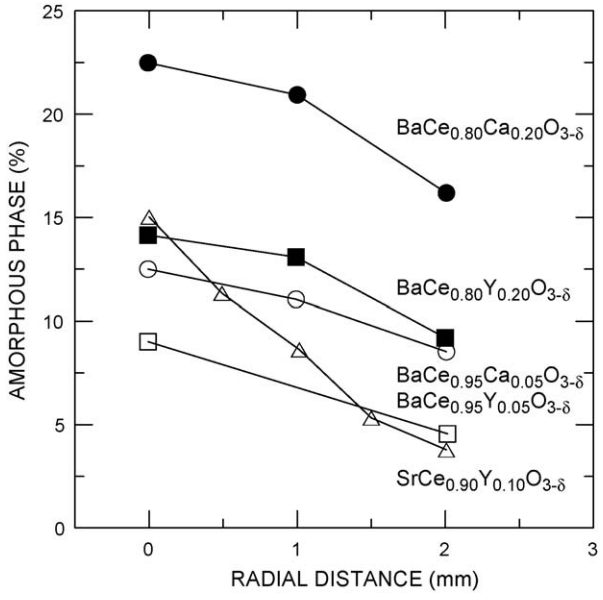

Fig. 2. Fraction surface of amorphous phase vs radial distance from the growth axis for as-fabricated Y-and Ca-doped $BaCeO_3$ and Y-doped $SrCeO_3$.

These findings are related with the processing technique. The laser radiation is absorbed in the specimen surface and the thermal energy diffuses into the crystal, leading to a temperature gradient in the solid; the crystallinity is then improved in the external surfaces.

EDX–SEM analyses revealed that the element concentrations inside the cells corresponded well with the expected composition of the perovskite compounds. However, aluminium cations were detected systematically in the amorphous phase (Fig. 3), with an average content of 3 mol%; in bulk, the mean Al content was about 0.5 mol%. In the barium and strontium cerates, a Ce deficit was found in the amorphous phase. Because the Al contamination was also found in crystals grown without alumina seeds, the origin of Al cations may be associated with the use of alumina crucibles for processing the polycrystalline precursors. On the other hand, the origin of the amorphous phase can be attributed to inhomogeneous evaporation of the precursor rods due to the elevated temperature in the molten zone during the LHFZ process. In a previous work on $LaAlO_3$ fibers grown by a similar laser-based technique,[28] the authors showed that such inhomogeneous evaporation was responsible for Al-rich phase inclusions observed inside the fibers. In this work, alumina contamination occurred during the sintering of the precursor rods. During melt growth, the perovskite solidified into cells and Al diffused to the melt, accumulating at the cell boundaries and forming thus an Al-rich and Ce-poor liquid that solidified as a glass.

3.2. High-temperature mechanical behavior

Fig. 4 compares the compressive stress–strain curves obtained at 1300 °C in air at constant strain rate $\dot{\varepsilon}$ of $5 \times 10^{-6}\,s^{-1}$ for all perovskite families and compositions studied; the axis loading was parallel to the growth direction. The maximum creep strength ranges from 100 to 380 MPa, being $BaCe_{0.95}Ca_{0.05}O_{3-\delta}$, $Sr_3(Ca_{1.18}Nb_{1.82})O_{9-\delta}$ and $SrZr_{0.8}Y_{0.2}O_{3-\delta}$ the strongest systems. Specimens fractured at strains lower than 10%, with the exception of compositions

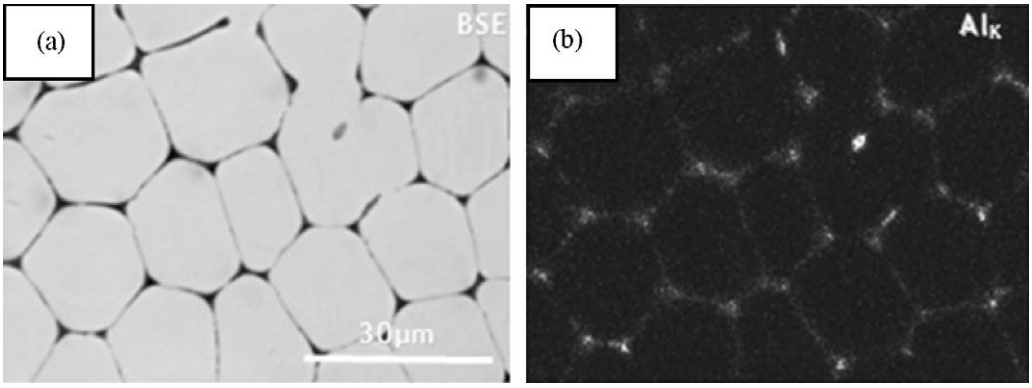

Fig. 3. (a) SEM micrograph of transversal cross-section of as-fabricated $SrCe_{0.90}Y_{0.10}O_{3-\delta}$ perovskite. (b) Corresponding EDX/SEM map showing the presence of Al cations along cell boundaries.

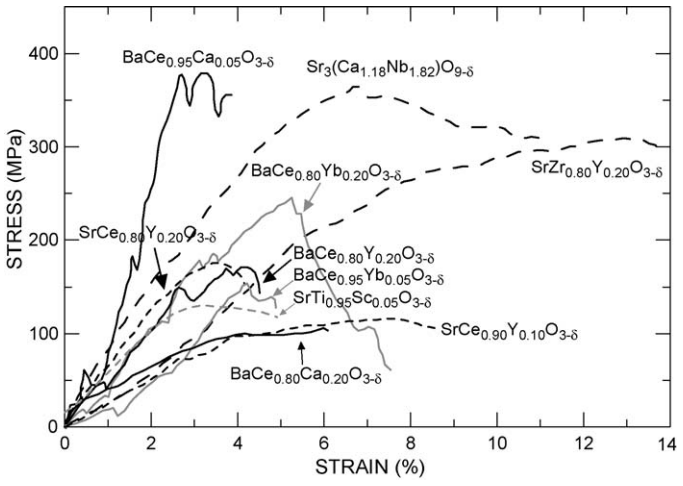

Fig. 4. Compressive stress vs strain curves at $T = 1300\,^{\circ}C$ and $\dot{\varepsilon} = 5 \times 10^{-6}\ s^{-1}$ in air for the melt grown perovskites fabricated in this work.

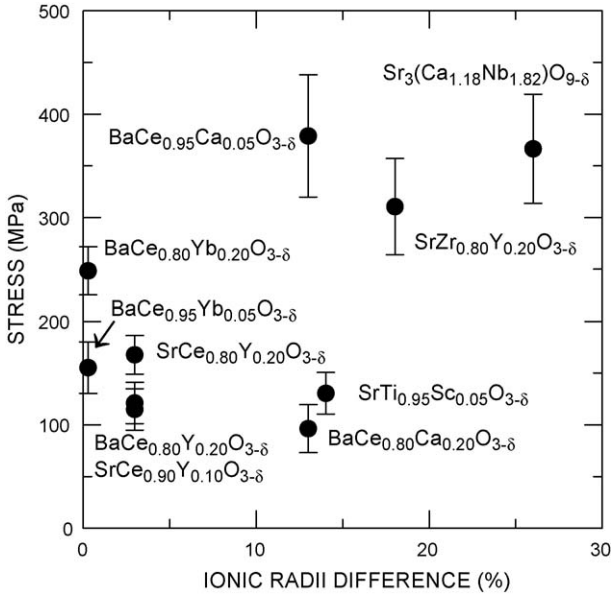

Fig. 5. Maximum creep strength vs difference in ionic radii between B^{4+} site and dopant for perovskite oxides deformed at 1300 °C and $\dot{\varepsilon} = 5 \times 10^{-6}\ s^{-1}$ in air; for the mixed perovskite $Sr_3(Ca_{1.18}Nb_{1.82})O_{9-\delta}$, the difference in ionic radii corresponds to Ca^{2+} and Nb^{5+}.

$Sr_3(Ca_{1.18}Nb_{1.82})O_{9-\delta}$ and $SrZr_{0.8}Y_{0.2}O_{3-\delta}$. This different behavior seems to be due to a higher damage tolerance more than to a larger plastic deformation accommodation, because the curves are rocky and a steady-state regime was not reached. In order to compare the creep strength of the various melt grown perovskites, the maximum stress attained during testing is plotted in Fig. 5 against the ionic radii[29] difference between B^{4+} site and dopant; for the mixed perovskite $Sr_3(Ca_{1.18}Nb_{1.82})O_{9-\delta}$, also included in Fig. 5, the difference in ionic radii corresponds to B' and B'' sites (i.e., Ca^{2+} and Nb^{5+}). The dependence of strength on ionic radii difference is not clear, especially if we consider that compounds with similar dopant concentration must be compared. However, it can be pointed out that the compositions in which dopants have the smallest difference on ionic radius (Y-doped $SrCeO_3$ and Yb-doped $BaCeO_3$) present strengths below 250 MPa, while the compositions in which dopants have the largest difference on ionic radius reach strengths up to 375 MPa.

Fig. 6 shows the plot of strength versus doping concentration. The strength increased with concentration for the systems with

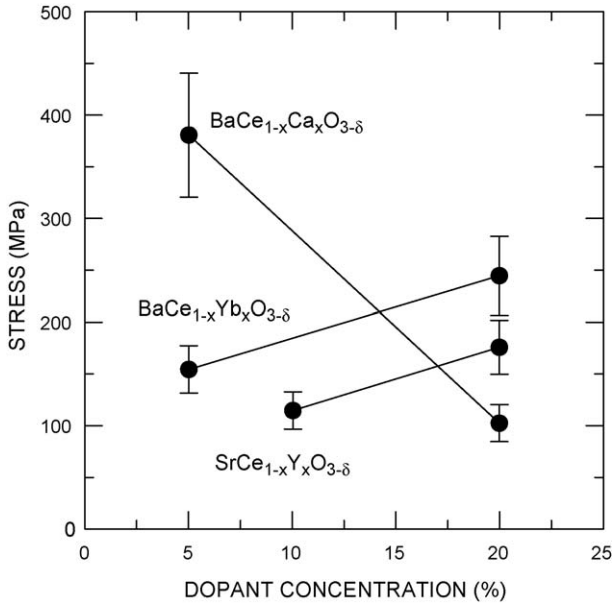

Fig. 6. Creep strength vs dopant concentration for Ca- and Yb-doped $BaCeO_3$ and Y-doped $SrCeO_3$ tested at $T = 1300\,^{\circ}C$ and $\dot{\varepsilon} = 5 \times 10^{-6}\ s^{-1}$ in air.

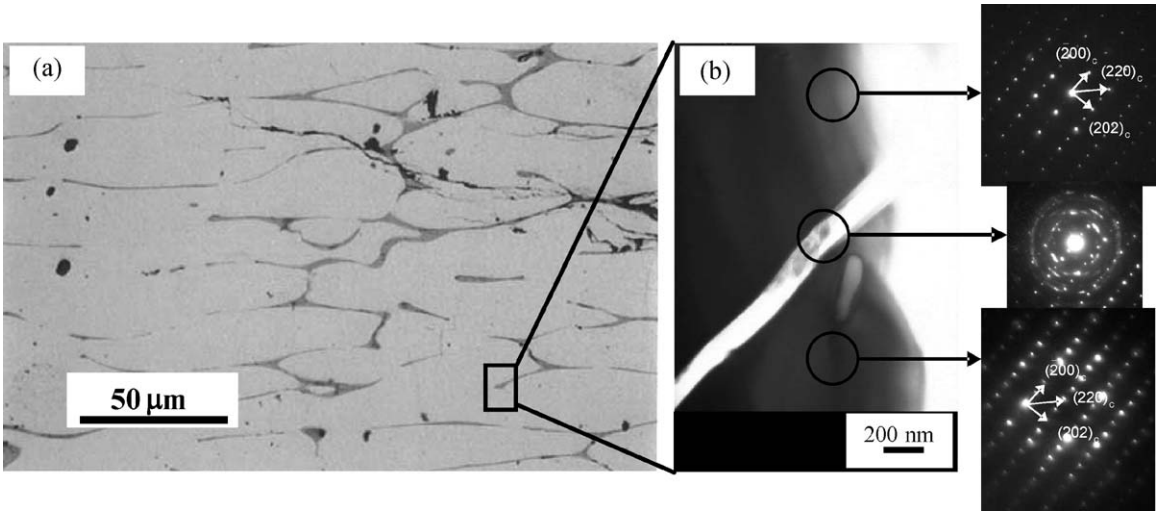

Fig. 7. SEM (a) and TEM (b) micrographs of a longitudinal cross-section of $SrCe_{0.90}Y_{0.10}O_{3-\delta}$ deformed at $T = 1300\,^{\circ}C$ (the loading axis is horizontal). Selected area diffraction patterns, indexed according to the pseudocubic prototype, of two adjacent grains and of the intercellular phase are shown.

trivalent dopants (Y-doped $SrCeO_3$ and Yb-doped $BaCeO_3$), but the opposite behavior was found for the compositions with divalent dopant (Ca-doped $BaCeO_3$). Y-doped $SrCeO_3$ and Yb-doped $BaCeO_3$ present smaller lattice deformation and lower oxygen vacant concentration than Ca-doped $BaCeO_3$ because each dopant atom generates half oxygen vacant. For this reason, it is plausible to think that the increase in strength with dopant is due to an increase of the lattice deformation caused by $[Y'_{Ce}]$ or $[Yb'_{Ce}]$ free defects, being the creation of complex defects involving O^{2-} vacancies, that tent to cancel this deformation. On the contrary, on Ca-doped $BaCeO_3$, it is likely that the formation of complex defects (like $[Ca''_{Ce} - V_O^{\bullet\bullet}]$) might dominate at high concentrations over the effect of free defects due to the larger amount of oxygen vacancies created, being then responsible for the decrease in strength.

Fig. 7 shows SEM and TEM micrographs of $SrCe_{0.9}Y_{0.1}O_{3-\delta}$ deformed at 1300 °C up to a final strain of 10%. Reduction of the intergranular phase could be observed after creep, which disappeared eventually from some boundaries; dark dots in Fig. 7(a) correspond with the remaining of intergranular boundaries, as detected by EDX/SEM. In addition, concurrent cell rotation and coalescence occurred during testing due to the redistribution of the amorphous phase. Fig. 7(b) shows two adjacent cells separated by a thin glassy phase; the corresponding selected area diffraction patterns (indexed according to the pseudocubic prototype[16]) indicate that both cells have practically the same crystallographic orientation, so cell coalescence could occur easily and may explain the small stress drops observed in the stress–strain curves (Fig. 4). Once the cells touched each other, further progress in plastic deformation was achieved by dislocation activity and eventually, microcracking; Fig. 7(a) shows a crack propagating initially in the less resistant phase (intercellular phase) and then into the cells. In a previous work on the high-temperature plastic deformation of $Sr_3(Ca_{1.18}Nb_{1.82})O_{9-\delta}$ carried out at constant load,[21] the authors concluded that the steady creep regime was controlled by a mixed diffusional/dislocation driven creep mechanism. In the present work, mechanical tests were conducted at constant strain rates much higher than those found under constant load ($\sim 10^{-7}\,s^{-1}$). Consequently, diffusion creep is unlikely to be important in the current experimental conditions, which could explain the lack of steady-state flow in the stress–strain curves. The high-temperature mechanical behavior of polycrystalline HTPC has been studied previously by several authors under experimental conditions similar to those used in this work. For $BaCe_{0.80}Y_{0.20}O_{3-\delta}$ with a grain size d of 9 μm and relative density of about 90%, Goretta et al.[30] reported a stress of 10 MPa, much lower than the value found in the present work (170 MPa, Fig. 4). Similarly, stresses lower than 10 MPa at 1300 °C and $\dot{\varepsilon} \approx 5 \times 10^{-6}\,s^{-1}$ have been reported in other perovskite oxides deformed in compression: $La_{0.9}Sr_{0.1}MnO_3$ ($d = 5$ μm),[31] $La_{0.8}Sr_{0.2}Ga_{0.85}Mg_{0.15}O_{2.825}$ ($d = 8$ μm)[32] and $BaTiO_3$ ($d = 20$–50 μm),[33] indicating that the LHFZ method is able to produce HTPC oxides with strong creep resistance.

4. Conclusions

Different families and compositions of high-temperature proton conducting perovskites were successfully fabricated by melt growth using the laser-heated floating zone technique: $SrCe_{1-x}Y_xO_{3-\delta}$ (with $x = 0.1$, 0.2), $BaCe_{1-x}M_xO_{3-\delta}$ (with M = Y, Yb and Ca; $x = 0.05$, 0.2), $Sr_3Ca_{1.18}Nb_{1.82}O_{9-\delta}$, $SrZr_{0.8}Y_{0.2}O_{3-\delta}$ and $SrTi_{0.95}Sc_{0.05}O_{3-\delta}$. The resulting materials have a unique microstructure with characteristic intermediate between single and polycrystals, consisting of strongly textured crystalline cells surrounded by an intercellular amorphous phase. Both the cells and the secondary phase decrease continuously in size with increasing the radial distance from the growth axis towards the external surface due to the large radial temperature gradients produced by the LHFZ method.

Compressive tests performed at constant strain rate in air at elevated temperatures have shown a redistribution of the amorphous phase during testing, accompanied by cell coalescence. The strength increases with increasing the difference in ionic

radii between dopant and host cations. Furthermore, the strength increased with doping concentration for the systems with trivalent dopants (Y-doped $SrCeO_3$ and Yb-doped $BaCeO_3$), but the opposite behavior was found for the composition with divalent dopant (Ca-doped $BaCeO_3$), which is explained by the formation of complex defects. Directionally solidified HTPC oxides exhibit higher strength than sintered HTPC polycrystals.

Acknowledgments

This material is based upon work supported by the European Office of Aerospace Research and Development, Air Force Office of Scientific Research, Air Force Research Laboratory, under Grant Nos. FA8655-03-1-3040 and F61775-02-WE001. Any opinions, findings and conclusions or recommendations expressed in this material are those of the author(s) and do not necessarily reflect the views of the European Office of Aerospace Research and Development, Air Force Office of Scientific Research, Air Force Research Laboratory. M.J. López-Robledo is grateful to the Junta de Andalucía (Spain) for a predoctoral grant.

References

1. Steele BC. Survey of materials selection for ceramic fuel cells. *Solid State Ionics* 1996;**86–88**:1223–34.
2. Hagawa T, Moe K, Hiramatsu T, Goto S. Design of electrodes for solid oxide fuel cells reactor. *Solid State Ionics* 1998;**106**:227–35.
3. Iwahara H, Uchida H, Tanaka S. High temperature type proton conductor based on $SrCeO_3$ and its application to solid electrolyte fuel cells. *Solid State Ionics* 1983;**9–10**:1021–5.
4. Iwahara H, Yajima T, Uchida H. Effect of ionic radii of dopants on mixed ionic conduction ($H^+ + O^{2-}$) in $BaCeO_3$-based electrolytes. *Solid State Ionics* 1994;**70–71**:267–71.
5. Uchida H, Maeda N, Iwahara H. Relation between proton and hole conduction in $SrCeO_3$-based solid electrolytes. *Solid State Ionics* 1983;**11**:117–24.
6. Guan J, Dorris SE, Balachandran U, Liu M. Transport properties of $BaCe_{0.95}Y_{0.05}O_{3-\alpha}$ mixed conductors for hydrogen separation. *Solid State Ionics* 1997;**100**:45–52.
7. Iwahara H, Esaka T, Uchida H, Maeda N. Proton conduction in sintered oxides and its application to steam electrolysis for hydrogen production. *Solid State Ionics* 1981;**3–4**:359–63.
8. Iwahara H. High temperature proton conductors based on perovskite-type oxides. In: Colomban P, editor. *Proton Conductors: Solids, Membranes and Gels—Materials and Devices*. Cambridge: Cambridge University Press; 1992. p. 122–37.
9. Nowick AS, Du Y. High-temperature protonic conductors with perovskite-related structures. *Solid State Ionics* 1995;**77**:137–46.
10. Reiche U, Arons RR, Schilling W. Investigation of n-type electronic defect in protonic conductor. *Solid State Ionics* 1996;**86–88**:639–45.
11. Ma G, Matsumoto H, Iwahara H. Ionic conduction and nonstoichiometry in non-doped $BaCeO_{3-\alpha}$. *Solid State Ionics* 1999;**122**:237–47.
12. Taniguchi N, Hatoh K, Niikura J, Gamo T. Proton conductive properties of gadolinium-doped barium cerates at high temperatures. *Solid State Ionics* 1992;**53–56**:998–1003.
13. Bonanos N. Transport study of the solid electrolyte $BaCe_{0.9}Gd_{0.1}O_{2.95}$ at high temperatures. *J Phys Chem Solids* 1993;**54**:867–70.
14. Flint SD, Hartmanova M, Jones JS, Slade RCT. Microstructure of Ca-doped barium cerate electrodes. *Solid State Ionics* 1996;**86–88**:679–83.
15. Llorca J, Orera VM. Directionally solidified eutectic ceramic oxides. *Prog Mater Sci* 2006;**51**:711–809.
16. Ramírez-Rico J, Lopez-Robledo MJ, de Arellano-López AR, Martínez-Fernández J, Sayir A. Fabrication and microstructure of directionally solidified $SrCe_{1-x}Y_xO_{3-\delta}$ ($x = 0.1, 0.2$) high temperature proton conductors. *J Eur Ceram Soc* 2006;**26**:3705–10.
17. Laguna-Bercero MA, Larrea A, Peña JI, Merino RI, Orera VM. Structured porous Ni- and Co-YSZ cermets fabricated from directionally solidified eutectic composites. *J Eur Ceram Soc* 2005;**25**:1455–62.
18. Sayir A, Farmer SC, Dickerson PO, Yun HM. High temperature mechanical properties of $Al_2O_3/ZrO_2(Y_2O_3)$ fibers. *Mater Res Soc Symp Proc* 1995;**365**:21–7.
19. Sayir A, Farmer SC. The effect of microstructure on mechanical properties of directionally solidified $Al_2O_3/ZrO_2(Y_2O_3)$ eutectics. *Acta Mater* 2000;**48**:4691–7.
20. López Robledo MJ, Pinto Gómez AR, Martínez Fernández J, de Arellano López AR, Sayir A. Microestructura y propiedades mecánicas de conductores protónicos de alta temperatura crecidos por fusión de zona flotante. *Bol Soc Esp Cer Vid* 2004;**43–4**:753–8.
21. López Robledo MJ, de Arellano López AR, Martínez Fernández J, Sayir A. Diffusion and creep of $Sr_3(Ca_{1.18}Nb_{1.82})O_{9-\delta}$. *Solid State Ionics* 2007;**178**:207–11.
22. Peña JI, Merino RI, Harlan NR, Larrea A, de la Fuente GF, Orera VM. Microstructure of Y_2O_3 doped Al_2O_3–ZrO_2 eutectics grown by the laser floating zone method. *J Eur Ceram Soc* 2002;**22**:2595–602.
23. Ranløv J, Lebech B, Nielsen K. Neutron diffraction investigation of the atomic defect structure of Y-doped $SrCeO_3$, a high-temperature protonic conductor. *J Mater Chem* 1995;**5**:743–7.
24. Phillips RJ, Bonanos N, Poulsen FW, Ahlgren EO. Structural and electrical characterisation of $SrCe_{1-x}Y_xO_{3-\delta}$. *Solid State Ionics* 1999;**125**:389–95.
25. Takeuchi K, Loong CK, Richardson Jr JW, Guan J, Dorris SE, Balachandran U. The crystal structures and phase transitions in Y-doped $BaCeO_3$: their dependence on Y concentration and hydrogen doping. *Solid State Ionics* 2000;**138**:63–77.
26. Mather GC, Islam MS. Defect and dopant properties of the $SrCeO_3$-based proton conductor. *Chem Mater* 2005;**17**:1736–44.
27. López Robledo MJ, Ramírez Rico J, Martínez Fernández J, de Arellano López AR, Sayir A. Microestructura y comportamiento plástico de perovsquitas conductoras protónicas de alta temperatura. *Bol Soc Esp Cer Vid* 2005;**44–5**:347–51.
28. Andreeta MRB, Andreeta ERM, Hernández AC. Laser-heated pedestal growth of colorless $LaAlO_3$ single crystal fiber. *J Cryst Growth* 2005;**275**:757–61.
29. Shannon RD. Revised effective ionic radii and systematic studies of interatomic distances in halides and chalcogenides. *Acta Cryst* 1976;**A32**:751–67.
30. Goretta KC, Park ET, Guan J, Balachandran U, Dorris SE, Routbort JL. Diffusional creep of $BaCe_{0.8}Y_{0.2}O_{3-\alpha}$ mixed conductors. *Solid State Ionics* 1998;**111**:295–9.
31. Wolfenstine J, Armstrong TR, Weber WJ, Boling-Risser MA, Goretta KC, Routbort JL. Elevated temperature deformation of fine-grained $La_{0.9}Sr_{0.1}MnO_3$. *J Mater Res* 1996;**11**:657–62.
32. Wolfenstine J. Rate-controlling species for creep of the solid state electrolyte doped lanthanum gallate. *Solid State Ionics* 1999;**126**:293–8.
33. Park ET, Nash P, Wolfenstine J, Goretta KC, Routbort JL. High-temperature creep of polycrystalline $BaTiO_3$. *J Mater Res* 1999;**14**:523–8.